PERGAMON

International Journal of Multiphase Flow 27 (2001) 119–145

International Journal of Multiphase Flow

www.elsevier.com/locate/ijmulflow

Slug-to-annular regime transitions in R-134a flowing through a vertical duct

P.F. Vassallo*, T.A. Trabold, R. Kumar, D.M. Considine

Lockheed Martin Corporation, P.O. Box 1072, Schenectady, New York 12301, USA

Received 11 February 1999; received in revised form 31 December 1999

Abstract

Measurements of pressure gradient, local void fraction and interfacial velocity were taken in R-134a flowing through a vertical duct to characterize the transition from slug to fully developed annular flow. The measurements were taken in both heated and adiabatic conditions for two system pressures and two mass flow rates. The adiabatic data showed that droplet entrainment was enhanced at the higher pressure so that a definite transition occurred between thick film flooding-type flow and thin film annular flow; when this situation occurred, a small decrease in pressure gradient was noted. At the same time, the local void profiles showed an inversion from a classical center-peaked slug distribution to a wall-peaked annular distribution. The effect was less evident at the lower pressure and flow rate, where transition was prolonged and less noticeable, and where a thicker transverse film existed in higher average void fractions. The heated data showed similar trends as the adiabatic data except that the heating action induced a more dramatic effect on the frictional pressure gradient near the slug-to-annular transition and caused the transition to occur at lower average void fractions. Published by Elsevier Science Ltd.

Keywords: Slug flow; Annular flow; Pressure drop; Void fraction; Flow regime transition

1. Introduction

A variety of flow regimes may occur in a flowing two-phase system as the void fraction is increased, including the bubbly, slug, annular, and mist regimes (Jones, 1992). The void fraction range over which each occurs is a function of conduit geometry, fluid properties and

* Corresponding author.

0301-9322/01/$ - see front matter. Published by Elsevier Science Ltd.
PII: S0301-9322(00)00009-4

system parameters (e.g., pressure, temperature, and mass flow rate). Considerable data exist which define flow regimes in air–water flows in tubes (Hewitt and Roberts, 1969; Taitel et al., 1980; Tutu, 1982), but less data is available for other systems.

The transitions between flow regimes do not occur sharply; rather, they occur over a void fraction range which again is a function of geometry, properties, and system parameters. Often, in these transitional flows, the pressure drop and heat transfer characteristics change, which may potentially impact system performance and should then be considered in system design. Of particular interest is the transition between the slug and annular regimes, commonly referred to as churn-turbulent flow. Many two-phase systems operate in the annular flow regime to optimize the heat transfer; it is therefore important to understand the behavior of the system in the transitional regime just below the operating condition. Knowledge of system behavior at higher void fractions (e.g., in the mist regime) is less important because dryout on the walls of the flow conduit is generally avoided.

The present study was undertaken to examine the slug to annular transition for two mass flow rates (w = 531.6 and 1063 kg/h) at two pressures (P = 1379 and 2413 kPa) for both adiabatic and heated flow. Measurements used to help characterize the transition included pressure gradient, local and average void fraction, and interfacial velocity. The working fluid for all the experiments was R-134a[1], one of the relatively new class of nonchlorinated refrigerant fluids which does not deplete the ozone layer. This fluid is widely used in heat exchangers, air conditioning and refrigeration systems, and is recommended as a replacement for R-113 and R-114. Aside from its practical importance, R-134a is also of scientific interest because of its very low liquid-to-vapor density ratio and low surface tension (7.3 and 0.0021 N/m, respectively, at 2.4 MPa). A description of testing in R-134a is available in Trabold et al. (1997).

2. Experimental description

2.1. Test section and loop

Key components of the experimental R-134a loop are a chiller and pressurizer to maintain the liquid phase at the inlet of a circulating canned rotor pump, a large CO_2 heat exchanger, loop heaters, high/low range throttle valves, flow meters, and a vertical test section. The test section, illustrated schematically in Fig. 1, is 1.22 m long, with an approximate aspect ratio of 20 and a hydraulic diameter of 4.8 mm. Optical access to the flow is provided by eight quartz windows, each 3.8 cm thick by 5.7 cm wide by 27.9 cm long. Transparent metallic oxide conductive films are vacuum deposited onto the inside surface of the windows to allow heat addition when current is supplied through the films. Between each pair of windows are 2.54 cm diameter inserts in the side of the test section. These inserts permit access to the flow for thermocouple rakes or Y-axis traversing hot-film anemometer (HFA) probes.

The instrument scanning mechanism (ISM) positions the gamma densitometer (GDS) along

[1] 1,1,1,2-tetrafluoroethane

the three axes: the Z-axis (horizontal scans along the test section spacing dimension), the Y-axis (horizontal scans transverse to the test section), and the X-axis (vertical, or streamwise position). The origin of the measurement axes is illustrated in Fig. 1. In order to measure void distributions in either the thickness (Z) or the width (Y) directions, the GDS can be rotated 90° about the test section. Both laser and gamma beam tests have shown that the ISM positioning accuracy is approximately ± 0.025 mm, with an uncertainty of ± 0.075 mm due to thermal expansion in the test section.

In the current experiments, the two-phase flow field was created by one of two methods: (1) phase change in the test section due to heat addition through the window heater strips, and (2) generating voids upstream of the test section with loop heaters. The second condition is referred to as adiabatic testing while the first is referred to as heated testing. The inlet temperature for the heated testing was controlled by means of a heater/cooler located upstream

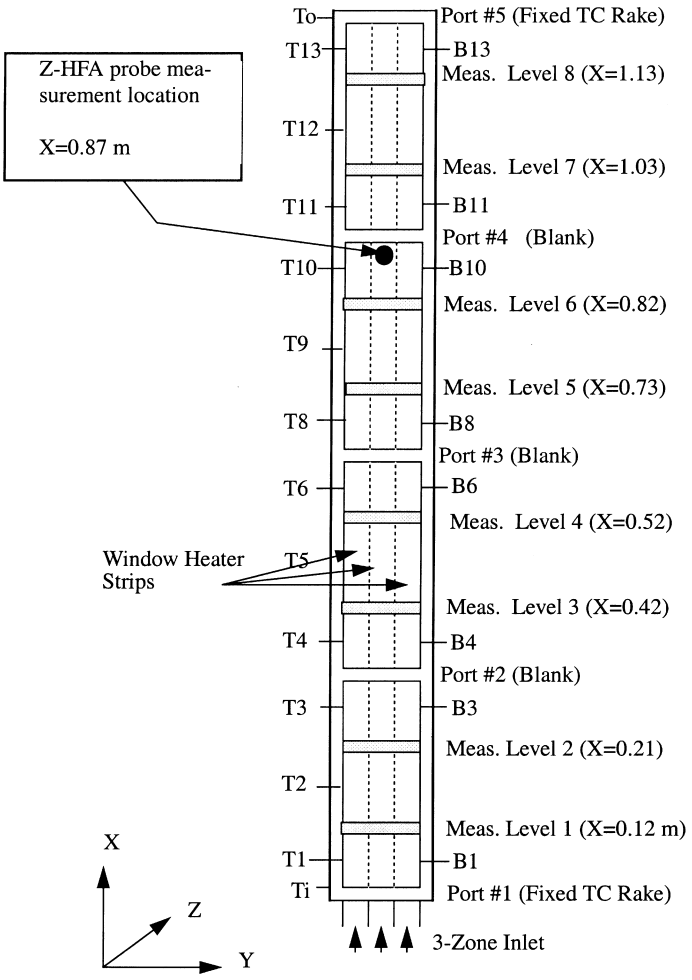

Fig. 1. Test section schematic, including GDS measurement levels, pressure tap locations (B1–B13, T1–T13) and HFA Z probe location.

of the test section inlet. Subcooled liquid was introduced to the test section and heat was applied uniformly to all eight windows. In this way, the net heat flux was held approximately constant over the entire test section length.

2.2. Test instrumentation

In order to examine the streamwise development of void fraction, GDS data were obtained at all available axial measurement positions (measurement Level 1 through 8 in Fig. 1). In addition to wide beam measurements of the cross-sectional average void fraction, narrow beam line-average edge scan data were obtained. Also, local void fraction and interfacial velocity data were acquired with a HFA dual-sensor probe mounted at $X = 0.87$ m, $Y = 0.03$ m (Z-traversing probe). Pressure drop data was taken in each window and across each Port, as shown in Fig. 1. Each instrument and associated analysis procedures are discussed in the following sections.

2.2.1. Pressure drop

2.2.1.1. Expression for pressure gradient. For steady flow in a constant cross section duct, the momentum equation can be recast to obtain the following expression for the pressure gradient in terms of its individual components (Hewitt, 1991):

$$-\frac{\mathrm{d}P}{\mathrm{d}X} = \frac{4\tau_0}{D} + G^2 \frac{\mathrm{d}}{\mathrm{d}X}\left[\frac{(1-x)^2}{\rho_{\mathrm{L}}(1-\epsilon_{\mathrm{G}})} + \frac{x^2}{\rho_{\mathrm{G}}\epsilon_{\mathrm{G}}}\right] + \rho_{2\phi} g \tag{1}$$

It signifies that total pressure gradient is the combination of frictional pressure gradient, acceleration pressure gradient, and gravitational pressure gradient, respectively, where

P = static pressure
X = axial distance
τ_0 = wall shear stress
D = hydraulic diameter
G = mass flux
x = flowing quality
ρ = liquid, gas or two-phase density
ϵ_{G} = gas void fraction

In adiabatic flow, the acceleration gradient is zero, and Eq. (1) is reduced to:

$$-\frac{\mathrm{d}P}{\mathrm{d}X} = \frac{f\Phi G^2}{2D\rho_{\mathrm{L}}} + \rho_{2\phi} g \tag{2}$$

The frictional pressure gradient in Eq. (2) is formulated as the single-phase frictional gradient (with friction factor, f) multiplied by the two-phase friction multiplier (Φ). In single-phase liquid flow, $\Phi = 1$ and $\rho_{2\phi} = \rho_{\mathrm{L}}$, while in single-phase gas flow, $\Phi = \rho_{\mathrm{L}}/\rho_{\mathrm{G}}$ and $\rho_{2\phi} = \rho_{\mathrm{G}}$. The Blasius relation for friction factor, f, in which for a smooth duct, $f = 0.316Re^{-0.25}$ may be used to calculate the singe-phase pressure gradient for all liquid or all gas flow.

2.2.1.2. Pressure gradient measurements. In the current test, pressure data were acquired for both heated and adiabatic testing at measurement locations shown in Fig. 1. Pressure taps T1–T13 were located on one edge of the test section; taps B1–B13 were located on the other edge. The pressure gradient in the adiabatic testing was determined by taking the average of the measured gradients in each of the four windows (for a total of eight measurements on the average). In the heated testing, the pressure gradient was obtained by taking separate averages of the two measured gradients in each window. The uncertainty in each incremental pressure drop measurement was ± 0.013 psi. The uncertainty in the average measurements, based on examination of repeated data was $\pm 3\%$.

The measured pressure drop includes gravity, friction and acceleration components. Eq. (1) may be used to determine the frictional component in adiabatic flow, and the acceleration component in heated flows, via analyses discussed more deeply in Sections 3.1.1 and 3.2.1.1.

2.3. Gamma densitometer system (GDS)

The gamma densitometer system (with a 9 curie Cesium source) provides a direct measurement of the density of the two-phase mixture in the path of the gamma beam through the relationship:

$$\rho_{2\phi} = \frac{\ln(I_0/I)}{\mu t} \tag{3}$$

where I_0 and μt are calibration constants obtained from gamma count measurements at each desired measurement position with an empty test section and a subcooled liquid filled test section. I is the count rate measured for the two-phase test condition. The two-phase density is related to the void fraction and vapor and liquid densities through the relationship:

$$\rho_{2\phi} = (1-\alpha)\rho_{\mathrm{L}} + \alpha\rho_{\mathrm{G}} \tag{4}$$

where α is the void fraction, ρ_{L} is the density of the liquid phase, and ρ_{G} is the density of the vapor phase. Solving for α yields:

$$\alpha = \frac{\rho_{\mathrm{L}} - \rho_{2\phi}}{\rho_{\mathrm{L}} - \rho_{\mathrm{G}}} \tag{5}$$

The liquid and vapor phase densities are determined from a database for R-134a saturation properties at the measured test section exit temperature.

The gamma beam width can be changed to accommodate either the narrow or wide beam dimension by rotating the source collimator with the collimator selector switch. The gamma beam exit collimator height is 1.9 cm for both the source collimator positions. The wide beam, when directed through the edge of the test section (wide beam edge measurement), interrogates the entire cross-sectional area and yields a measurement of the cross-sectional average void fraction. A spacing (Z) dimension void fraction data scan is obtained using the narrow beam directed through the test section edge (narrow beam edge scan). The effective gamma beam width at the test section for a narrow beam edge scan is 0.43 mm. Each measurement location overlaps the adjacent one by 0.13 mm and the fluid is interrogated to within about 0.15 mm of the heated test section walls.

Two minute counting times were used for both wide beam and narrow beam edge measurements. The wide beam edge measurement was obtained three times and averaged. The statistic precision ($\pm 2\sigma$) for each individual wide beam measurement (2 min count) is ± 0.017 in void fraction. For each narrow beam edge measurement (2 min count), the precision is ± 0.032.

2.2.3. Hot-film anemometry (HFA)

The constant temperature hot-film anemometer technique has been used previously for various thermal-hydraulics measurements and is described in detail by Trabold et al. (1997). For the present test sequence, a dual-sensor probe was installed for void fraction measurements along one spacing (Z) scan. This HFA probe is comprised of two active sensing elements which are separated in the streamwise (X) direction by a known distance, d_s. The HFA probes used in the present study had platinum film sensors with 25 μm diameter and 254 μm active length. The sensor separation distance of the two probes was about 2.5 mm. The time record for the upstream sensor can be analyzed to provide the local void fraction. An analysis method has been developed which automatically calculates the threshold voltage, and then applies the method of de Carvalho and Bergles (1992) to provide the void fraction data. This approach has been validated in various adiabatic and wall-heated experiments by comparing integrated average HFA data to line-average GDS void fraction measurements.

The use of two sensors permits acquisition of interfacial velocity measurements based on the cross-correlation between two output voltage signals:

$$E(\tau) = \lim_{T\to\infty} \frac{1}{T} \int_0^T V_1(t) V_2(t+\tau)\, \mathrm{d}t \tag{6}$$

The peak in the $E(t)$ versus time plot corresponds to the most probable time required for a gas–liquid interface to travel between the HFA sensors, from which the mean interfacial velocity may be calculated by

$$V_i = \frac{d_s}{t_{E(\tau)\max}} \tag{7}$$

where d_s is the spacing between upstream and downstream HFA sensors. This method of interfacial velocity measurement has been validated in previous subcooled boiling and annular flow experiments, through comparison with nonintrusive laser Doppler velocimetry (LDV) measurements (Trabold et al., 1997).

3. Results and discussion

The conditions for the experiments were selected to cover a range of pressures (P = 1379 and 2413 kPa) for both heated and adiabatic flow. The mass flow rates, w = 531.6 and 1063 kg/h, were chosen because, at these flow rates, the frictional component of pressure gradient is large and its relationship to void fraction is likely to indicate flow regime transitions. The void fraction range for the adiabatic test cases extended from the slug regime to the annular regime.

The void fraction range in the heated test cases extended from subcooled boiling at the test section inlet to slug or annular flow at the test section exit, depending on the heat addition.

The stability of the loop was evaluated by examining how the flow conditions varied throughout the course of testing. Table 1 shows the averages of the actual values of flow rate, pressure and inlet temperature for all pertinent runs, as well as the standard deviation from the average. The average values were all within 1% of nominal values and the relatively low deviation indicates good repeatability.

In the following sections, the adiabatic and heated data, in particular their relationship to the transition from slug to annular flow, is described. Selected data plots of pressure gradient, void fraction and interfacial velocity are presented which highlight the discussion.

3.1. Adiabatic test results

3.1.1. Data trends and observations. The frictional pressure gradient data is plotted in Fig. 2. The gravitational component has been subtracted from the measured total gradient using Eq. (2) as:

$$\frac{\mathrm{d}P}{\mathrm{d}X_{\text{friction}}} = \frac{\mathrm{d}P}{\mathrm{d}X_{\text{total}}} - \left[(1-\bar{\alpha})\rho_{\mathrm{L}} + \bar{\alpha}\rho_{\mathrm{G}}\right] \tag{8}$$

where ρ_{G} and ρ_{L} are the gas and liquid phase densities at saturation and $\bar{\alpha}$ is the average void fraction measured with the GDS at $X = 1.13$ m. The densities were obtained from DuPont's R-134a database as follows: for $P = 1379$ kPa, $\rho_{\mathrm{L}} = 1094$ kg/m^3, $\rho_{\mathrm{G}} = 67.5$ kg/m^3; for $P = 2413$ kPa, $\rho_{\mathrm{L}} = 951$ kg/m^3, $\rho_{\mathrm{G}} = 131$ kg/m^3. Included in Fig. 2 are values of single-phase liquid and gas pressure gradients calculated using the Blasius relation for smooth ducts, as described in Section 2.2.1.1. Measurements of single-phase liquid pressure gradient agree well with the predictions. Single-phase gas flow pressure drop could not be obtained in these tests, but the data trends at high void fractions are consistent with the predicted gas flow values.

The pressure gradient for $\alpha > 0.4$ is higher at $P = 1379$ kPa than it is at $P = 2413$ kPa because the vapor density is lower. Because of this, the gas phase velocity is significantly higher

Table 1
Average flow conditions, nominal vs. actual[a]

Condition	Nominal value	Number of runs for statistics[a]	Mean value	Standard deviation
Flow rate	531.6 kg/h (1017 kg/s m^2)	31	532.5 kg/h	5.1 kg/h
Flow rate	1063 kg/h (2034 kg/s m^2)	30	1058 kg/h	8.8 kg/h
Inlet pressure	1379 kPa	29	1384 kPa	9.0 kPa
Inlet pressure	2413 kPa	32	2426 kPa	9.7 kPa
Inlet temperature at $P = 200$ psi	48.9°C	8	49.2°C	0.44°C
Inlet temperature at $P = 350$ psi	73.9°C	8	74.1°C	0.17°C

[a] The number of runs for flow and pressure included both heated and adiabatic cases; for inlet temperature, only the heated cases were considered because the adiabatic cases were saturated at the inlet.

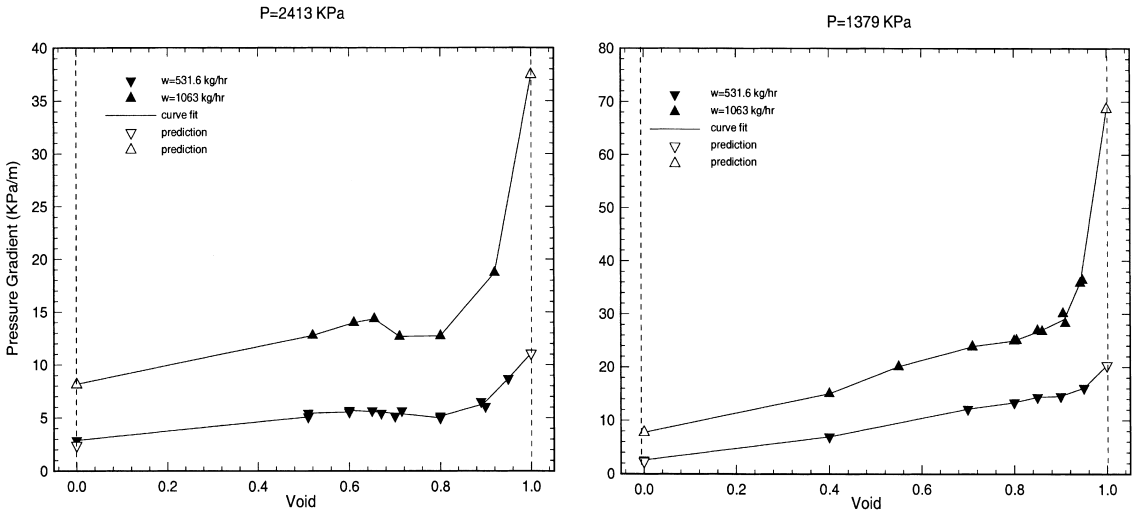

Fig. 2. Frictional pressure gradient data measured in adiabatic flow. The predicted points were determined using the Blasius relation for friction factor for smooth ducts.

at $P = 1379$ kPa, increasing the interfacial friction. Measurements of interfacial velocity, presented in Figs. 3 and 4, show clearly that the core velocity is higher at $P = 1379$ kPa for a given mass flow rate and void fraction. As the void fraction increases, the gas phase velocity increases, resulting in an increase in the frictional pressure gradient.

The data in Fig. 2 show a general increasing trend with void fraction; however, in the range $0.65 < \alpha < 0.75$ at $P = 2413$ kPa, a definite local decrease in pressure gradient is observed.

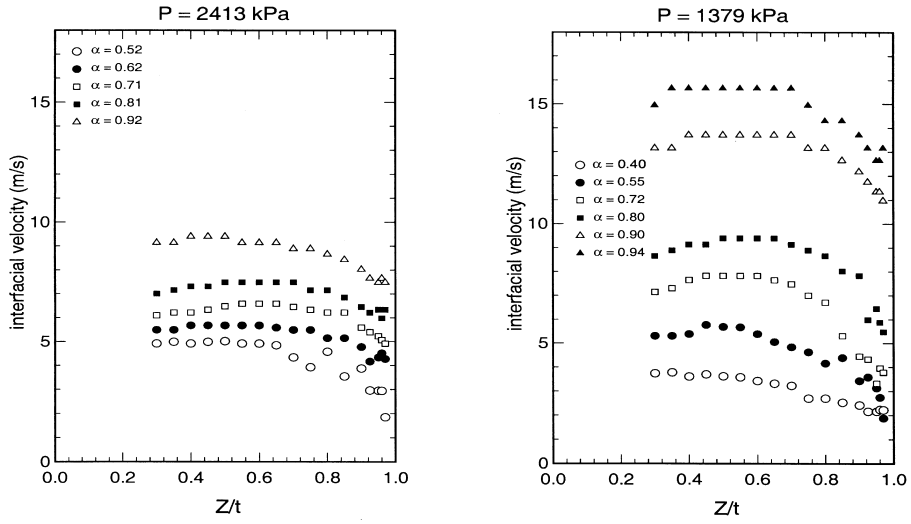

Fig. 3. Interfacial HFA velocity measurements across the test section thickness dimension for $w = 1063$ kg/h, adiabatic flow.

The decrease is seen to correspond with a flow regime change from a churn-turbulent flow into a more smoothly defined annular flow. This is confirmed by examining the measured void distribution in the test section thickness dimension, as shown in Figs. 5–7. The profiles for $\alpha < 0.6$ are predominantly center peaked, representative of slug or churn-turbulent flow. At $\alpha > 0.7$, the void profiles become wall peaked, indicating a regime change into annular flow with a large fraction of droplets in the core and a thin liquid film on the walls. The asymmetric distribution for $0.6 < \alpha < 0.7$ is due to the instability of the transitional regime. Here, the flow demonstrates 'metastable' behavior, where a slight change in the inlet conditions allows the void to peak near either test section wall.

The instability of the transitional regime is demonstrated by the line-averaged GDS void profiles in Fig. 6 for $0.5 < \alpha < 0.7$. The profiles were taken at different times during the test sequence; each profile was acquired for the same inlet and boundary conditions except for a slight variation in inlet transverse flow distribution. The data is repeatable at $\alpha = 0.5$ and 0.7, but at $\alpha = 0.6$ the profile shifts from a right peaked void distribution to a left peaked distribution. The data therefore show that the void distribution in the transitional regime is very sensitive to inlet conditions, while the distributions in the other, more stable, regimes are not.

Local HFA data is included in Fig. 6 for $w = 531.6$ kg/h and $P = 2413$ kPa. At the higher flow rate, where convection becomes significant, it was impossible to obtain accurate HFA measurements due to unstable baseline voltage levels in the HFA signals. Both HFA and GDS measurements in Figs. 5 and 6 show similar trends; the magnitude of void fraction measured with the HFA is generally larger than that obtained with the GDS because the former is a local measure in the transverse center of the test section, while the latter is an integrated average. At high system pressures in a high aspect ratio geometry, liquid will always be present

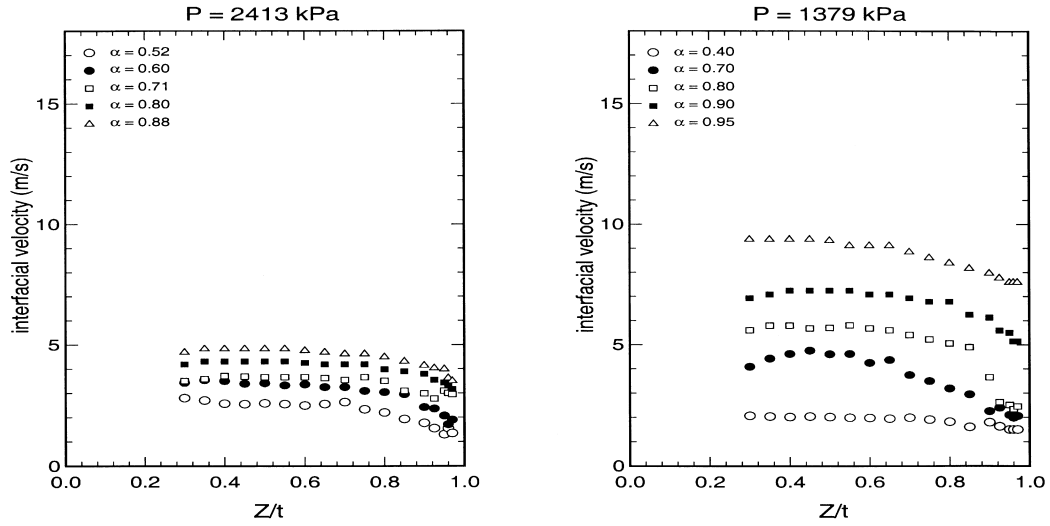

Fig. 4. Interfacial HFA velocity measurements across the test section thickness dimension for $w = 531.6$ kg/h, adiabatic flow.

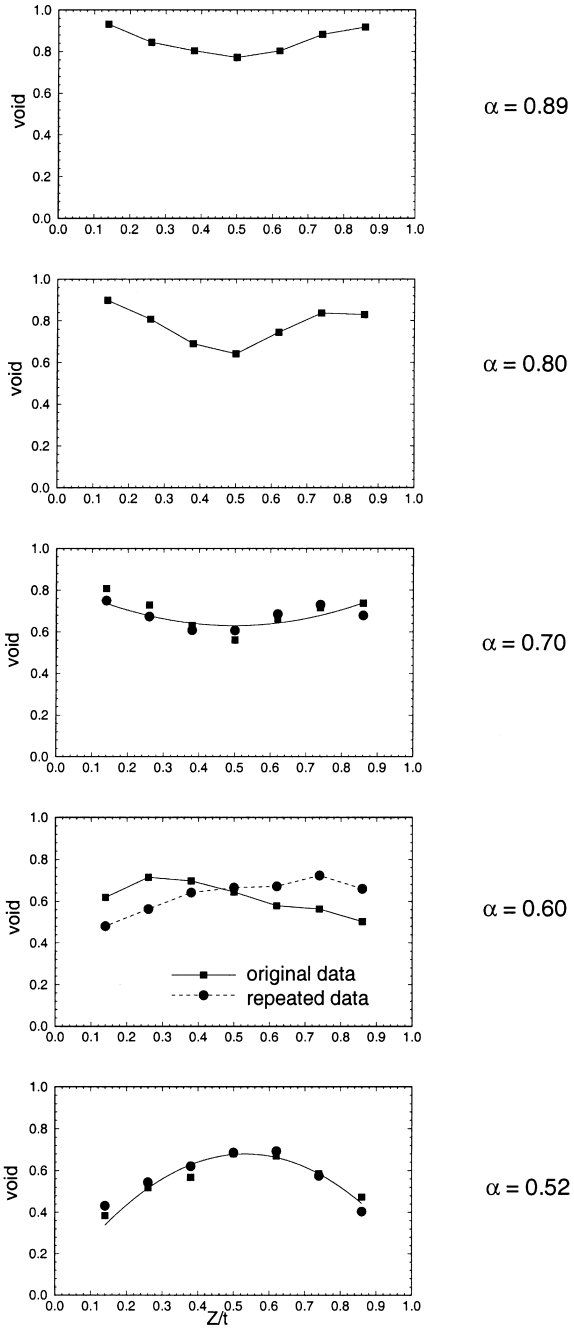

Fig. 5. Line average void distribution in test section thickness dimension at $X = 0.82$ m as measured with the gamma densitometer for $w = 531.6$ kg/h, $P = 2413$ kPa, adiabatic flow. Measurements of edge average void fraction at test section exit are included at right.

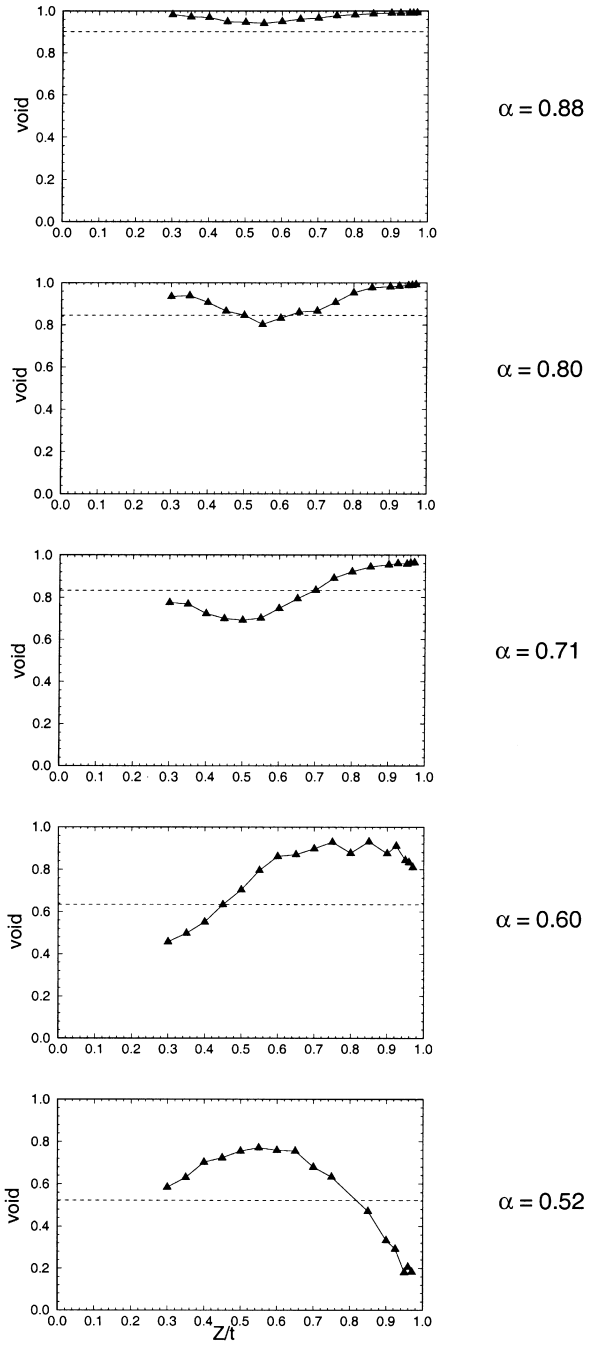

Fig. 6. Local void distribution in test section thickness dimension at $X = 0.82$ m, $Y = 0.03$ m as measured with the HFA probe for $w = 531.6$ kg/h, $P = 2413$ kPa, adiabatic flow. Measurements of GDS edge average void fraction at test section exit are included at right. Measurements of GDS line average void fraction at $Y = 0.03$ m are shown as dashed lines.

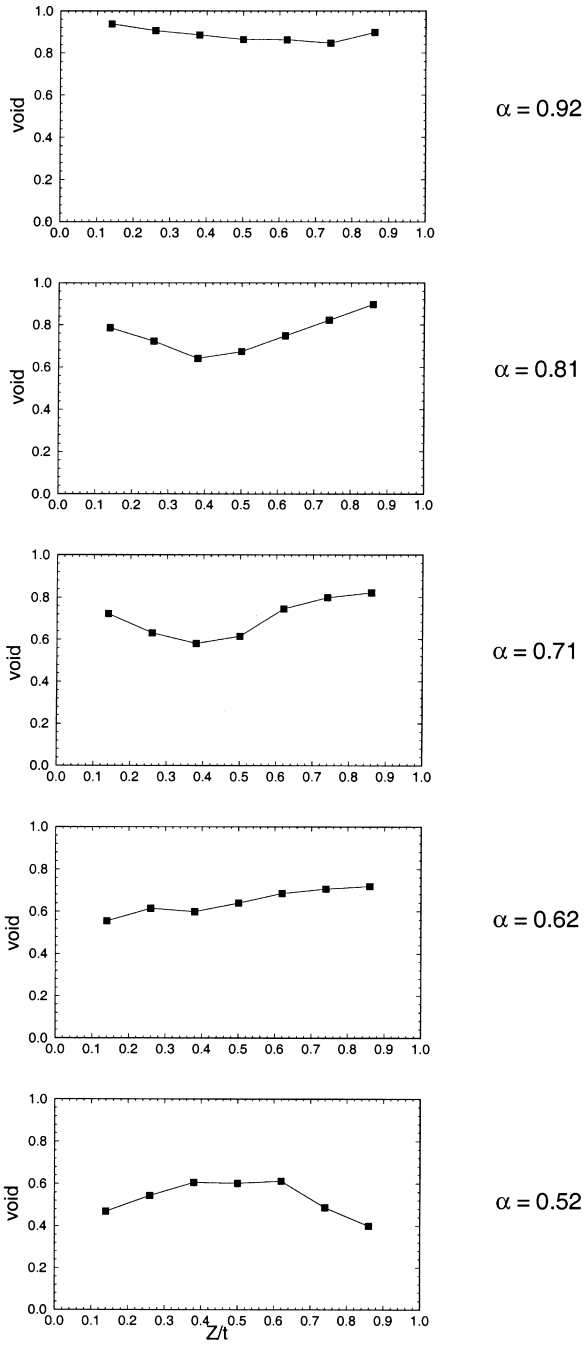

Fig. 7. Line average void distribution in test section thickness dimension at $X = 0.82$ m as measured with the gamma densitometer for $w = 1063$ kg/h, $P = 2413$ kPa, adiabatic flow. Measurements of edge average void fraction at test section exit are included at right.

in the test section edges, and therefore, the local void in the center is expected to be somewhat higher than the integrated average.

3.1.2. Flow mechanisms during transition. The mechanism responsible for the local decrease in pressure gradient during the transition into annular flow is believed to be similar to the mechanism observed by Hewitt et al. (1965) in air–water flow. In their study, water was introduced along the vertical middle circumference of a cylindrical tube as air was forced vertically through the tube. At high gas flow rates, the liquid was carried along with the gas and flowed upwards. As the gas flow was decreased, the film began to periodically reserve direction until, at the lowest gas flow rates, the falling film condition was reached. Measurements of pressure drop were taken over the entire range of gas flow rates and revealed a local minimum where the film began to change direction. Hewitt et al. demonstrated, using a laminar film analysis, that this minimum corresponded approximately to the condition in which the wall shear stress was close to zero. As the gas flow was reduced, the wall shear stress fluctuated in a manner to give both positive and negative stress distributions at the wall. The liquid flowed partly down forming a 'bulge' and then was periodically swept away by the gas flow, forming a series of large waves on the gas–liquid interface and creating a larger shear stress at the wall. Eventually, as the gas flow was further reduced, the down-flowing liquid could no longer be swept away by the gas and the pressure gradient decreased.

Although no falling film condition existed in the current test sequence, a similar argument can be made for the existence of a local minimum in pressure gradient near the transition into annular flow. During the churn-turbulent transition, flooding-type waves are formed which periodically transport the liquid upwards near the walls. These waves are formed during the breakdown of large vapor slugs into the vapor core via liquid bridge breakup. During this process, considerable rearranging of the fluid occurs which eventually leads to a thin liquid film. As noted by Govan et al. (1991), the average interfacial friction is much higher in the churn-turbulent regime than it would be in the annular regime for a film of equivalent thickness with no flooding-type waves present. Thus, when the liquid film first becomes stable and flows upward, with no local flow reversals, the frictional pressure gradient drops. As the void fraction increases beyond this point, the continuous gas phase core velocity increases, the liquid film thins, and the frictional pressure gradient begins to rise. This explanation is consistent with the observed trends in the data. Hereafter, this type of transition, which occurs during the last stage of the transition from slug to annular flow, is called 'thin-film transition'.

At 2413 kPa, where a dip in the pressure gradient is observed, a corresponding dip in void fraction occurs in the core of the flow (Figs. 2, 5 and 7). The void fraction dip is caused by the disintegration of liquid bridges into droplets in the transition regime. The droplets thus formed appear to have a larger concentration as the system pressure and flow rate increase. This trend can be attributed to entrainment mechanisms in the flow, whereby continuous liquid on the walls of the test section is converted to dispersed droplets within the gas core. Two pertinent entrainment mechanisms have been observed and modeled from the literature, including liquid bridge breakup (as derived from Pilch and Erdman (1987)) and liquid film entrainment (Kataoka and Ishii, 1982). The former mechanism, described above, is expected to dominate in the slug or churn-turbulent regime. As the flow approaches annular, the second mechanism

becomes more prominent, in which the high velocity gas phase "tears" liquid droplets from the surface of the liquid films.

Based on the functional form of the entrainment models, the entrainment rate for a given flow rate and void fraction level is enhanced at higher pressures where the gas density is higher and the liquid surface tension is lower. Also, the entrainment rate increases with flow rate because of the increase in gas phase velocity. The data, in general, support these conclusions; at $P = 1379$ kPa, $w = 531.6$ kg/h (Figs. 8 and 9), the void distribution in the thickness dimension maintains a center-peaked distribution in higher void fractions than at $P = 2413$ kPa, indicating that a thicker film exists on the test section walls. Only at the very highest void fractions is there any indication of wall peaked distributions. It therefore appears that the slug–annular transition regime is extended into higher void fractions as the pressure is reduced, consistent with observations made by Hosler (1967) in his study of low pressure steam–water flow. The data for $P = 1379$ kPa, $w = 1063$ kg/h (Figs. 10 and 11) show some asymmetry at the beginning of the thin-film transition, which is consistent with a much higher gas phase velocity in the core.

As a general summary, the adiabatic data show that entrainment is enhanced at high pressures so that a definite transition occurs between thick film flooding-type flow and thin film annular flow. When this situation occurs, a small decrease in pressure gradient is noted. The effect is less evident at lower pressures and lower flow rates, where the transition is extended and a thicker transverse film exists in higher void fractions.

3.2. Heated test results

The relationship between void distribution and pressure drop in the adiabatic flows brought to light some interesting flow features which have not been well documented in the literature. It is important to determine what similarities exist between adiabatic flows and wall-heated flows. The purpose of the experiments discussed in this section was to evaluate these similarities by uniformly heating the test section windows to reach similar flow conditions as in the previous adiabatic tests.

3.2.1. Pressure gradient data. The pressure gradient data, excluding the gravity component, for the wall-heated testing is plotted in Fig. 12. Each set of four data points connected by a line represents data taken at a given pressure, inlet temperature, mass flux and power at four axial positions in the test section. The maximum void fraction for each flow condition was obtained by incrementally increasing wall heat until dryout was nearly achieved at the test section exit. Several general trends are observed in Fig. 12: (1) the pressure gradient for the heated conditions is higher than the adiabatic conditions at the same mass flow rate and void fraction, and (2) the heated pressure gradient increases as the wall heat increases for the same average void fraction. Both of these effects can be attributed to the contribution of the acceleration pressure gradient term in Eq. (1) to the total pressure gradient. In the heated cases, the cross section averaged void fraction and flow quality increase axially, increasing the pressure drop compared to the adiabatic conditions at the same average void fraction.

Acceleration pressure gradient. The magnitude of the acceleration pressure gradient may be estimated by using Eq. (1) and pertinent measured data. An energy balance in the test section yields:

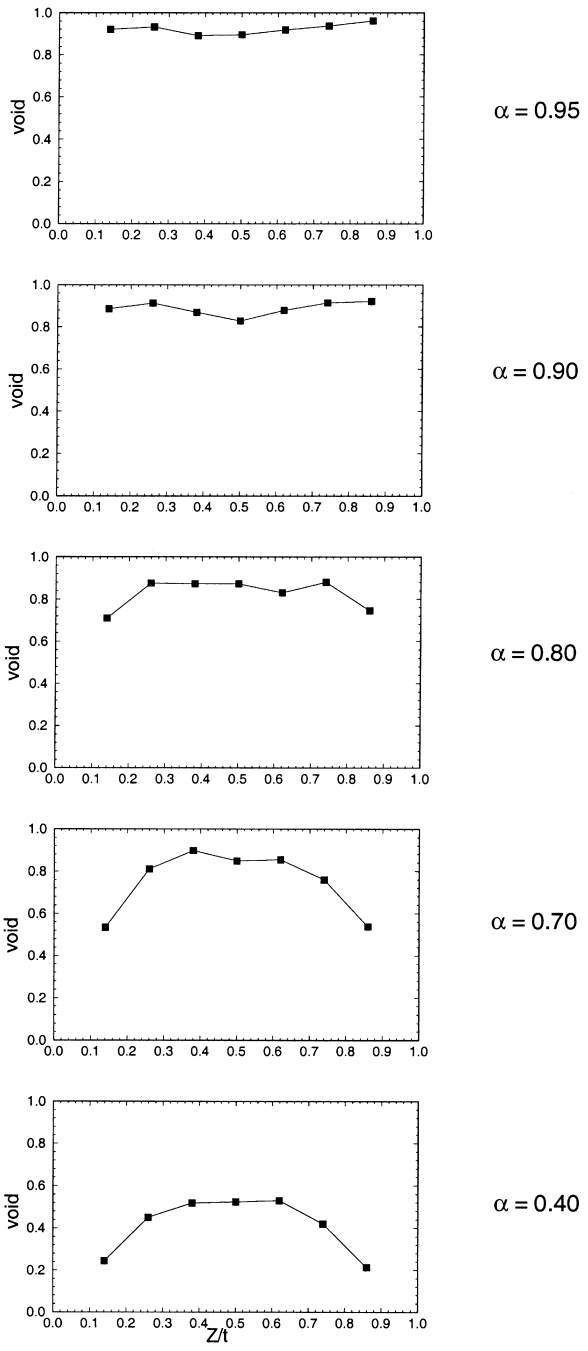

Fig. 8. Line average void distribution in test section thickness dimension at $X = 0.82$ m as measured with the gamma densitometer for $w = 531.6$ kg/h, $P = 1379$ kPa, adiabatic flow. Measurements of edge average void fraction at test section exit are included at right.

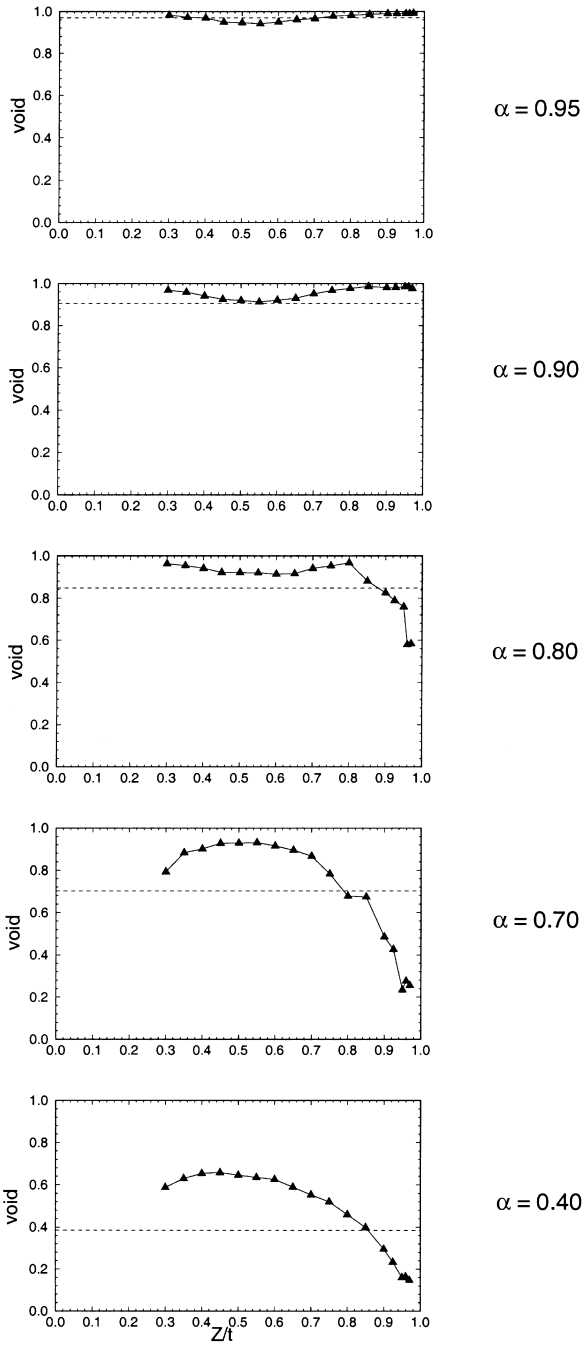

Fig. 9. Local void distribution in test section thickness dimension at $X = 0.82$ m, $Y = 0.03$ m as measured with the HFA probe for $w = 531.6$ kg/h, $P = 1379$ kPa, adiabatic flow. Measurements of GDS edge average void fraction at test section exit are included at right. Measurements of GDS line average void fraction at $Y = 0.03$ m are shown as dashed lines.

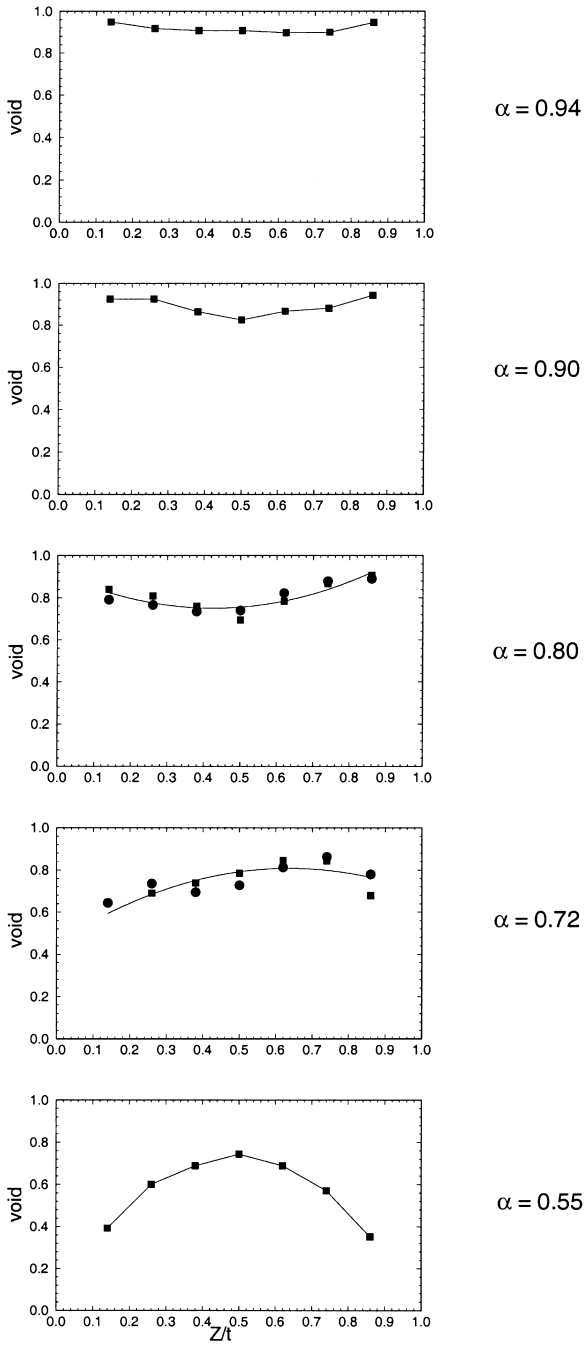

Fig. 10. Line average void distribution in test section thickness dimension at $X = 0.82$ m as measured with the gamma densitometer for $w = 1063$ kg/h, $P = 1379$ kPa, adiabatic flow. Measurements of edge average void fraction at test section exit are included at right.

$$x_e(X) = \frac{h_{in} - h_f}{h_{fg}} + \left(\frac{Q}{\dot{m} h_{fg} L}\right) X \tag{9}$$

where

$x_e(X)$ is the equilibrium quality at a given axial location,

h_{in}, h_f, h_{fg} are the inlet and saturated liquid enthalpies and the latent heat of vaporization,

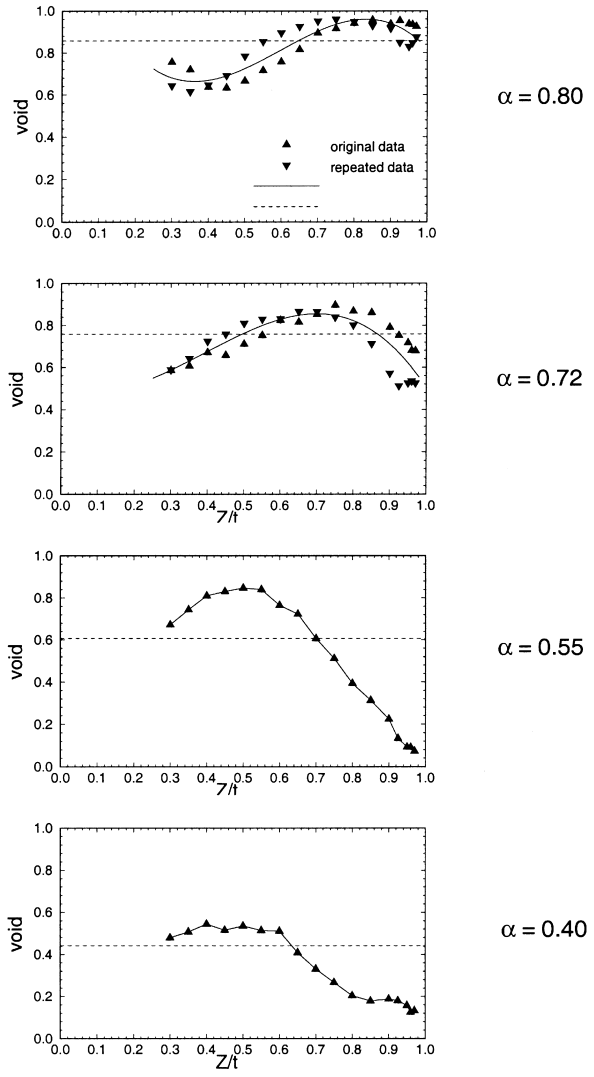

Fig. 11. Local void distribution in test section thickness dimension at $X = 0.82$ m, $Y = 0.03$ m as measured with the HFA probe for $w = 1063$ kg/h, $P = 1379$ kPa, adiabatic flow. Measurements of GDS edge average void fraction at test section exit are included at right. Measurements of GDS line average void fraction at $Y = 0.03$ m are shown as dashed lines.

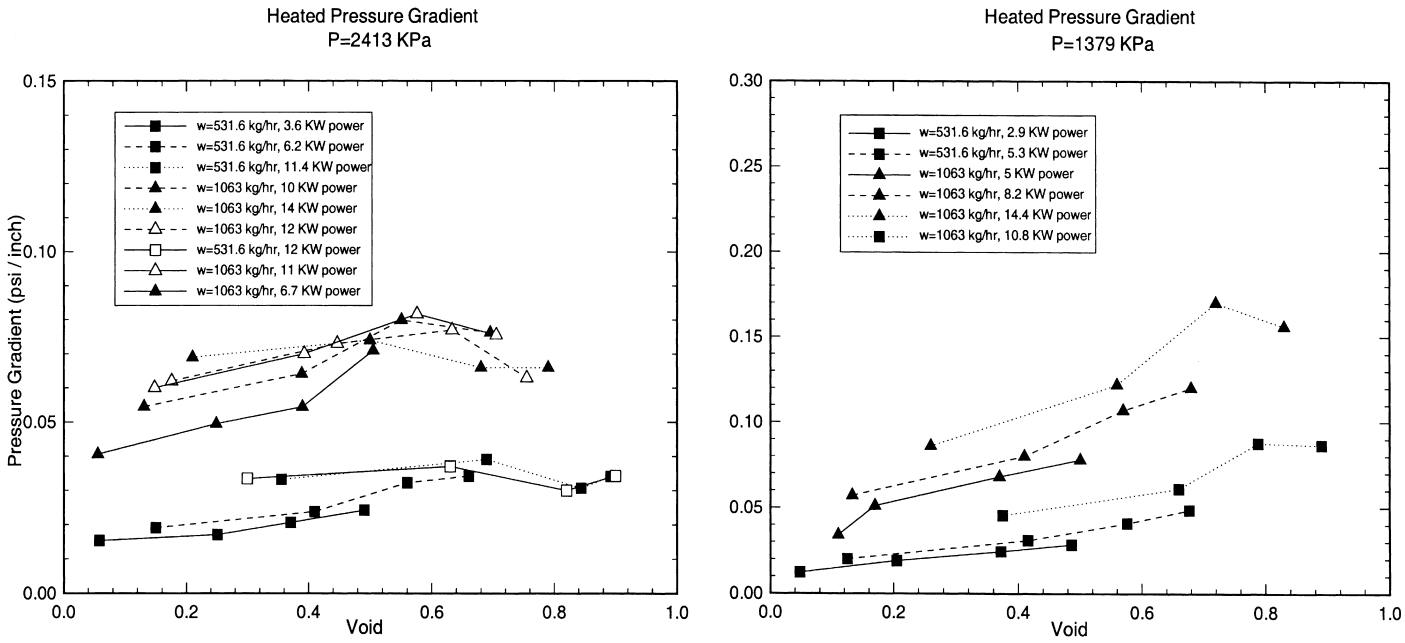

Fig. 12. Pressure gradient data (excluding gravity) measured in heated flow. The exit pressure, mass flow rate and test section heater power is indicated for each test run.

Q is the total test section power,
$\dot{m}$ is the mass flow rate, and
L is the heated length.

The total power is assumed to be uniformly applied across the entire test section. In order to use Eq. (1), the flowing quality must be computed. This is done by using the profile-fit model of Levy (1966), which is a well regarded model for the cases of uniform heat flux:

$$x(X) = x_e(X) - x_e\left(X_{\bar{h}}\right)\exp\left[\frac{x_e(X)}{x_e\left(X_{\bar{h}}\right)} - 1\right] \tag{10}$$

where $x_e(X_{\bar{h}})$ is the equilibrium quality at the point of net vapor generation. Net vapor generation refers to the location in the test section where significant boiling occurs. If the inlet flow is saturated, then boiling occurs immediately. As the inlet subcooling is increased, the point of net vapor generation occurs later in the test section. An expression for the enthalpy at which significant boiling occurs was derived by Kurul and Podowski (1991) as:

$$\bar{h} = h_f - \left\{1 + \left[-0.044\Psi\exp(-0.022\Psi) + \exp(-0.051\Psi)\right]\right\}\left\{154\frac{Q}{\dot{m}}\right\} \tag{11}$$

where

$$\Psi = \frac{\dot{m}\Delta h_{in}}{Q} \tag{12}$$

so that

$$x_e\left(X_{\bar{h}}\right) = \frac{\bar{h} - h_f}{h_{fg}} \tag{13}$$

Now, Eq. (1) may be used to obtain the acceleration component as follows. First, the flowing quality is computed at the eight axial locations in the test section corresponding to the GDS void fraction measurement locations. Next, the acceleration derivative term in Eq. (1) is computed numerically in each of the four test section windows. This derivative is evaluated at the center of each window (see Fig. 1) and corresponds with the average of the local pressure measurements. Subtracting the acceleration component and gravitational component from the total measured gradient yields the frictional component of pressure gradient in the heated conditions, which may be readily compared to the adiabatic measurements.

3.2.2. Data trends and observations. A comparison of the frictional pressure gradient in the heated conditions to the adiabatic conditions is made in Figs. 13 and 14. In general, the frictional pressure gradient in the heated flows compares well with that in adiabatic flows for $P =$ 1379 kPa. At the highest heat flux conditions, there is a drop in the frictional pressure gradient near $\alpha = 0.75$. An examination of the void fraction profiles (Figs. 15 and 16) reveals that the void distribution changes from a center-peaked distribution to a wall-peaked distribution near $\alpha = 0.75$. Thus, there appears to be a correspondence between the dip in frictional pressure gra-

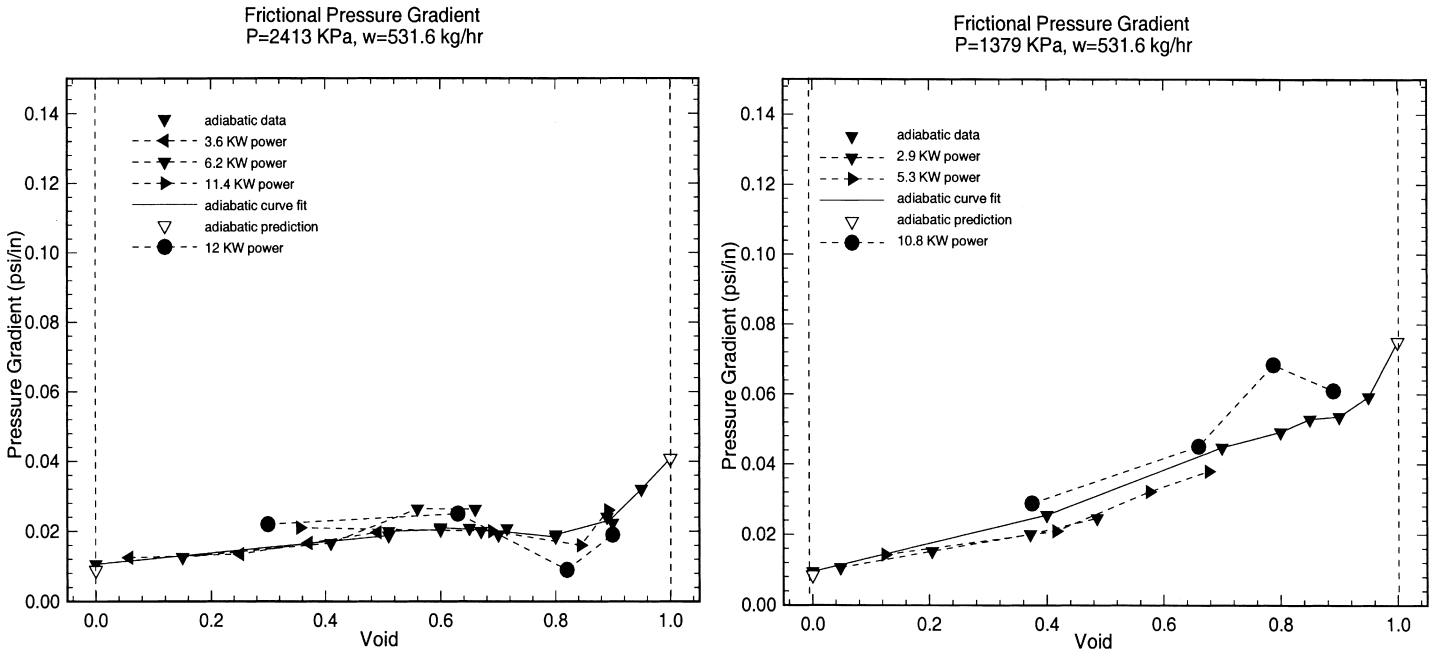

Fig. 13. Comparison of frictional pressure gradient measured in adiabatic flow with frictional pressure gradient calculated in heated flow for w = 531.6 kg/h.

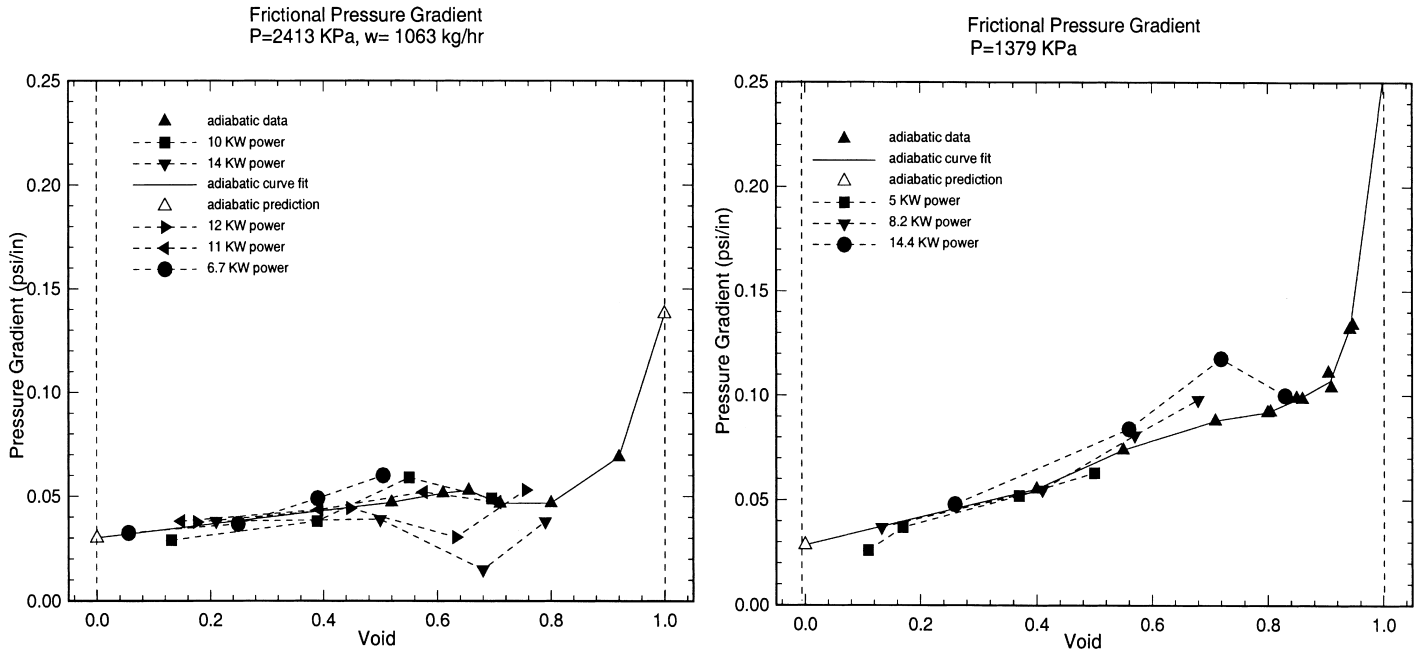

Fig. 14. Comparison of frictional pressure gradient measured in adiabatic flow with frictional pressure gradient calculated in heated flow for w = 1063 kg/h.

dient in the heated conditions and adiabatic conditions when the void fraction profile changes character. However, for the adiabatic conditions at $P = 1379$ kPa, there was no noticeable dip in frictional pressure gradient when the void profile changed from center to wall-peaked. It therefore appears that the heating action induces a more dramatic effect on the frictional pressure gradient near the slug-to-annular transition as compared to the adiabatic cases. In particular, for $P = 1379$ kPa, the frictional pressure gradient increases over that measured in adiabatic flows immediately preceding the local minima.

The reason for the increase in frictional pressure gradient may be related to bubble nucleation at the walls as the flow approaches the thin-film transition. The film is thicker at lower pressures and can support the existence of an increased number of bubbles. These bubbles interact with the film, increasing the local turbulence level and, therefore, increasing the effective wall roughness. As the effective wall roughness increases, so too does the frictional component of pressure gradient. Similar behavior has been observed in air–water bubbly flows (Marie et al., 1997). The effect is enhanced at higher liquid velocities, which explains why,

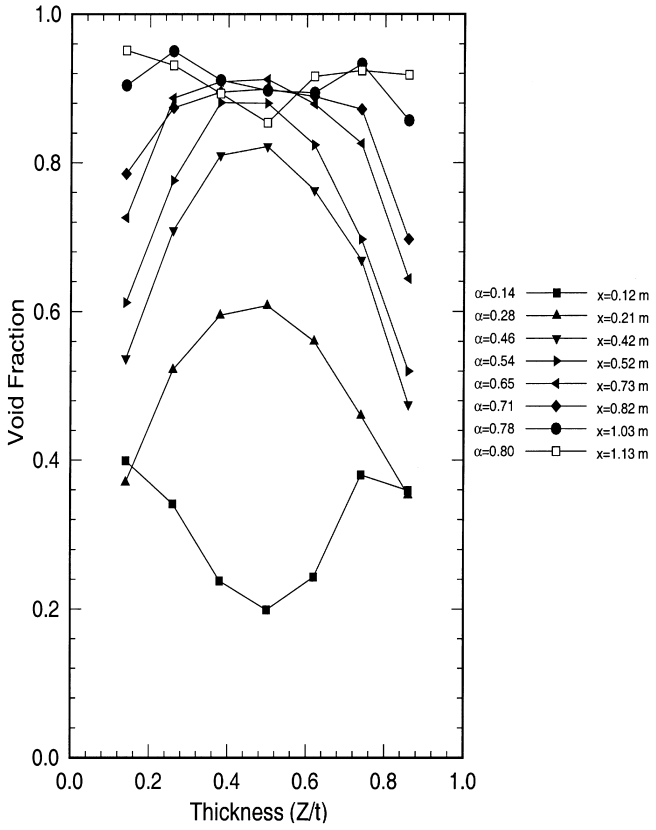

Fig. 15. Line average void distribution in test section thickness dimension as measured with the gamma densitometer for $w = 531.6$ kg/h, $P = 1379$ kPa, $Q = 10.8$ kW, $T_{in} = 48.9$°C. Measurements of edge average void fraction at given X elevations are included at right.

referring back to Figs. 15 and 16, the heated frictional pressure gradient for $\alpha < 0.6$ is close in magnitude to that measured in adiabatic flow (with no bubbles being generated at the walls).

Although the magnitude of the heated frictional pressure gradient does not fall significantly below the gradient measured in adiabatic flow for $P = 1379$ kPa, no such trend is observed for $P = 2413$ kPa (as seen in Figs. 13 and 14). In fact, there is a progressive departure from the adiabatic trendlines as the pressure and flow rate increase such that for $w = 1063$ kg/h, $P = 2413$ kPa, $\alpha \sim 0.6$ and $Q = 14$ kW, the frictional pressure gradient is noticeably less than the adiabatic data. At the local minima, the void distributions in the thickness dimension (presented in Figs. 17 and 18) show a shift from a center-peaked distribution to a wall-peaked distribution. Therefore, the dip in frictional gradient once again indicates a thin-film transition into annular flow. The indication is more obvious here, at high pressure, as the calculated frictional gradient drops quite sharply.

The reason the calculated values of frictional gradient fall below the adiabatic measurements is most likely due to the dramatic change in flow character within the test section between the pressure tap locations. For example, at $w = 1063$ kg/h, $P = 2413$ kPa, and $\alpha \sim 0.6$ the void

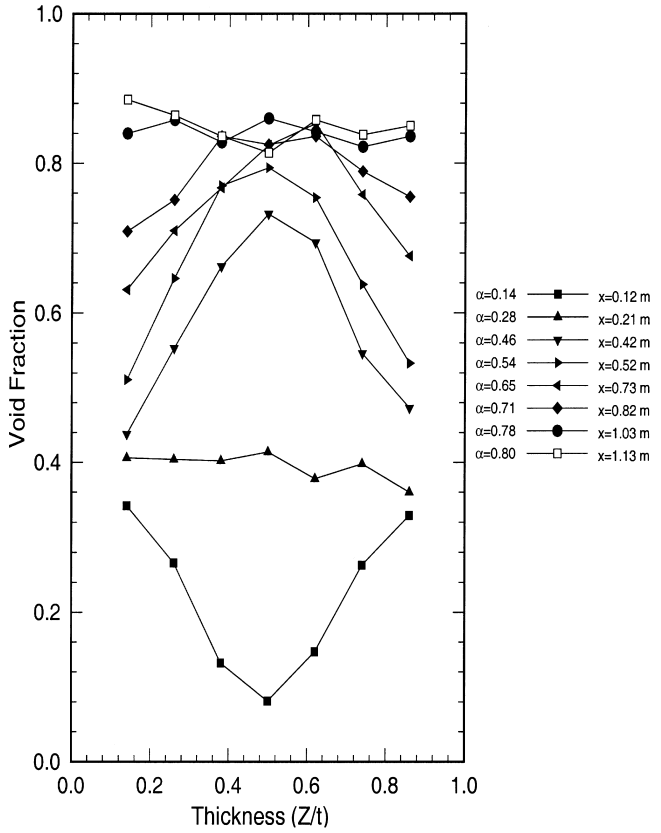

Fig. 16. Line average void distribution in test section thickness dimension as measured with the gamma densitometer for $w = 1063$ kg/h, $P = 1379$ kPa, $Q = 14.4$ kW, $T_{in} = 48.9°C$. Measurements of edge average void fraction at given X elevations are included at right.

distribution at $X = 0.73$ m (just above the upstream pressure tap) is transitional in nature, while the void distribution at $X = 0.82$ m (just below the downstream pressure tap) is inverted, or annular in nature. If, as stated previously, the minimum frictional gradient occurs near the transition into annular flow and increases thereafter, the absolute pressure at the upstream tap would be relatively low and the pressure at the downstream tap would be relatively high. The gradient obtained by subtraction is therefore smaller in magnitude than a local measurement would be at the transition location.

4. Final remarks on transition study

The slug–annular transition in R-134a flowing through a vertical duct was characterized for two pressures and two mass flow rates for both heated and adiabatic flow. The transitions at $P = 2413$ kPa were shorter and easier to identify than at $P = 1379$ kPa because the void profile inverted quickly at the higher pressure. An inverted profile is a sure indication of an annular-

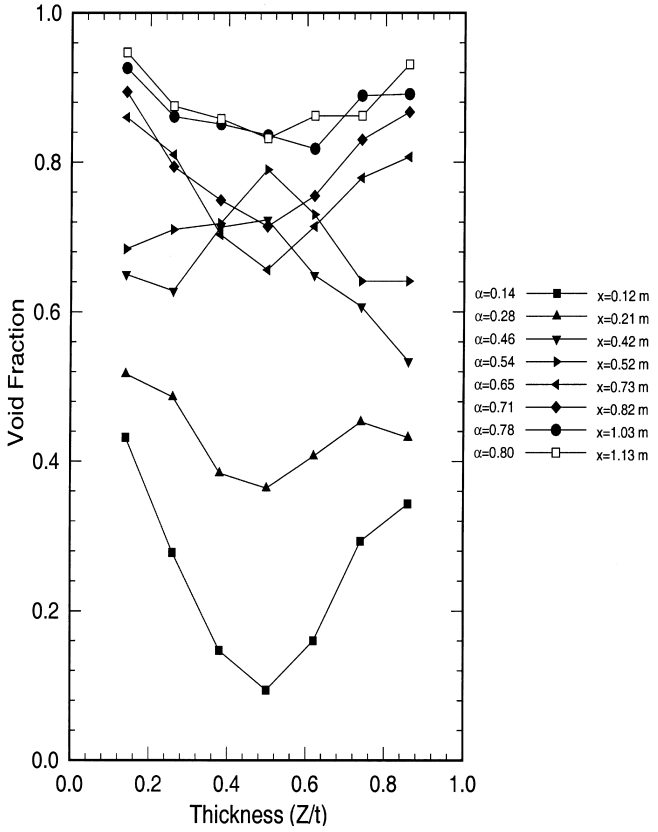

Fig. 17. Line average void distribution in test section thickness dimension as measured with the gamma densitometer for $w = 531.6$ kg/h, $P = 2413$ kPa, $Q = 12$ kW, $T_{in} = 73.9°C$. Measurements of edge average void fraction at given X elevations are included at right.

type flow. However, as it is still possible to have an annular-type flow with a center-peaked void profile, it is difficult to determine where the annular transition occurs at the lower pressure. At high enough void fractions, inverted profiles were observed at the lower pressure, so a better identifier in comparing the two pressure conditions was the transition into a thin-film annular flow, defined by the inverted void profiles. Table 2 summarizes the estimated void fractions where this transition is believed to occur (within an uncertainty of approximately $\pm 5\%$ void). The void fractions correspond closely to the locations of maximum pressure gradient and the average void fraction where the local void profiles were at, or near, inversion. Although this is a subjective classification, the data in Table 2 shows fairly systematic trends: (1) heating causes thin-film transition to occur at a lower void fraction compared to adiabatic cases, (2) thin-film transition occurs at higher void fractions as the pressure is reduced and (3) thin-film transition occurs at higher void fractions as the mass flow rate is reduced. All of these trends are consistent with observations made previously.

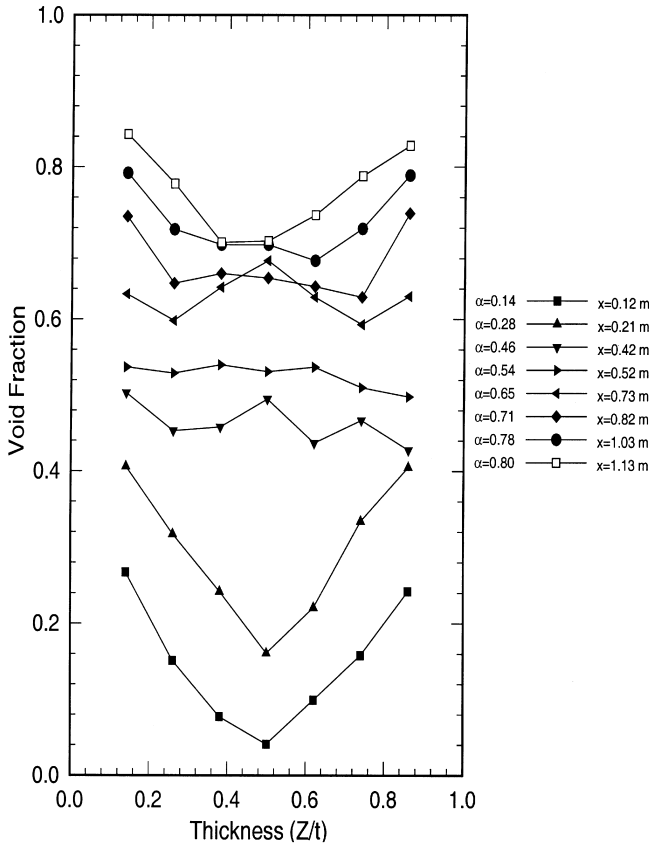

Fig. 18. Line average void distribution in test section thickness dimension as measured with the gamma densitometer for $w = 1063$ kg/h, $P = 2413$ kPa, $Q = 14$ kW, $T_{in} = 73.9°C$. Measurements of edge average void fraction at given X elevations are included at right.

Table 2
Estimated void fraction at thin-film annular transition

Flow (kg/h)	Pressure (kPa)	Condition	Void
1063	2413	Adiabatic	0.7
1063	2413	Heated	0.6
1063	1379	Adiabatic	0.8
1063	1379	Heated	0.75
531.6	2413	Adiabatic	0.7
531.6	2413	Heated	0.65
531.6	1379	Adiabatic	0.9
531.6	1379	heated	0.8

Acknowledgements

The authors gratefully acknowledge the efforts of L. Jandzio and W.O. Morris for their technical support during data acquisition and analysis and of G.J. Kirouac for his guidance and support of the fundamental experimental program.

References

de Carvalho, R., Bergles, A.E., 1992. The pool nucleate boiling and critical heat flux of vertically oriented, small heaters boiling on one side. Rennselaer Polytechnic Institute, Heat Transfer Laboratory Report HTL-12.

Govan, A.H., Hewitt, G.F., Richter, H.J., Scott, A., 1991. Flooding and churn flow in vertical pipes. Int. J. Multiphase Flow 17, 27–44.

Hewitt, G.F., Roberts, D.N., 1969. Studies of two-phase patterns by simultaneous X-ray and flash photography. AERE-M 2159. HMSO.

Hewitt, G.F., 1991. Annular flow phenomena. Proc. of the Japan Society of Multiphase Flow — Waves and Turbulence in Multiphase Flow and its Application. pp. 126–154.

Hewitt, G.F., Lacey, P.M.C., Nicholls, B., 1965. Transitions in Film Flow in a Vertical Tube. AERE-R 4614.

Hosler, E.R., 1967. Flow Patterns in High Pressure Two-Phase (Steam–Water) Flow With Heat Addition. Westinghouse, Report WAPD-TM-658.

Jones, O.C., 1992. Elements of two-phase flow. In: Lahey, R.T. (Ed.), Boiling Heat Transfer. Elsevier, Amsterdam.

Kataoka, I., Ishii, M., 1982. NUREG/CR-2885, ANL-82-44.

Kurul, N., Podowski, M.Z., 1991. On the modelling of multidimensional effects in boiling channels. ANS Proc. HTC-5.

Levy, S., 1966. Forced convection subcooled boiling — prediction of vapor volumetric fraction. GEAP-5157.

Marie, J.L., Moursali, E., Tran-Cong, S., 1997. Similarity law and turbulence intensity profiles in a bubbly boundary layer at low void fractions. Int. J. Multiphase Flow 23, 227–247.

Pilch, M., Erdman, C.A., 1987. Use of breakup time data and velocity history data to predict the maximum size of stable fragments for acceleration-induced breakup of a liquid drop. Int. J. Multiphase Flow 13, 741–757.

Taitel, Y., Bornea, D., Dukler, A.E., 1980. Modelling flow pattern transitions for steady upward gas–liquid flow in vertical tubes. AICHE J. 26, 345–354.

Trabold, T.A., Moore, W.E., Morris, W.O., 1997. Hot-film anemometer measurements in adiabatic two-phase refrigerant flow through a vertical duct. In: Proceedings of the ASME Fluids Engineering Conference. Vancouver, BC, Paper FEDSM97-3518.

Tutu, N.K., 1982. Pressure fluctuations and flow pattern recognition in vertical two-phase gas–liquid flows. Int. J. Multiphase Flow 8, 443–447.